








Mapping the Magnetic Field of Flare Coronal Loops

D. Kuridze^{1,2,3} , M. Mathioudakis² , H. Morgan¹, R. Oliver^{4,5} , L. Kleint^{6,7} , T. V. Zaqarashvili^{3,8,9}, A. Reid², J. Koza¹⁰ ,
M. G. Löfdahl¹¹, T. Hillberg¹¹, V. Kukhianidze³, and A. Hanslmeier⁹

¹ Institute of Mathematics, Physics and Computer Science, Aberystwyth University, Ceredigion, Cymru, SY23 3BZ, UK; dak21@aber.ac.uk

² Astrophysics Research Centre, School of Mathematics and Physics, Queen's University Belfast, Belfast BT7 1NN, UK

³ Abastumani Astrophysical Observatory at Ilia State University, 3/5 Cholokashvili Avenue, 0162, Tbilisi, Georgia

⁴ Departament de Física, Universitat de les Illes Balears, E-07122 Palma de Mallorca, Spain

⁵ Institut d'Aplicacions Computacionals de Codi Comunitari (IAC3), Universitat de les Illes Balears, Spain

⁶ University of Applied Sciences and Arts Northwestern Switzerland, Bahnhofstrasse 6, 5210 Windisch, Switzerland

⁷ Leibniz-Institut für Sonnenphysik (KIS), Schöneckstrasse 6, D-79104 Freiburg, Germany

⁸ Space Research Institute, Austrian Academy of Sciences, Schmiedlstrasse 6, A-8042 Graz, Austria

⁹ IGAM, Institute of Physics, University of Graz, Universitätsplatz 5, A-8010 Graz, Austria

¹⁰ Astronomical Institute, Slovak Academy of Sciences, 059 60 Tatranska Lomnica, Slovakia

¹¹ Institute for Solar Physics, Department of Astronomy, Stockholm University, Albanova University Centre, SE-106 91 Stockholm, Sweden

Received 2019 January 15; revised 2019 February 11; accepted 2019 February 19; published 2019 March 29

Abstract

Here, we report on the unique observation of flaring coronal loops at the solar limb using high-resolution imaging spectropolarimetry from the Swedish 1 m Solar Telescope. The vantage position, orientation, and nature of the chromospheric material that filled the flare loops allowed us to determine their magnetic field with unprecedented accuracy using the weak-field approximation method. Our analysis reveals coronal magnetic field strengths as high as 350 G at heights up to 25 Mm above the solar limb. These measurements are substantially higher than a number of previous estimates and may have considerable implications for our current understanding of the extended solar atmosphere.

Key words: instrumentation: polarimeters – Sun: chromosphere – Sun: corona – Sun: flares – Sun: magnetic fields – techniques: polarimetric

Supporting material: animation

1. Introduction

The structure and dynamics of the most energetic events in the solar outer atmosphere such as flares, eruptions, coronal loops, and CMEs are controlled by the magnetic field. This field is created deep in the solar interior by dynamo processes, transported outwards by magnetic buoyancy, and permeates the photosphere in dense flux ropes—giving the familiar appearance of sunspots and pores, associated with coronal active regions (ARs). Over time, this intense emergent field diffuses throughout the photosphere and fills the solar chromosphere and corona, dominating the movement and behavior of the hot plasma. The majority of the EUV/X-ray emission is from loops of plasma entrained along closed fields. Measurements of the magnetic field in loops is key to our understanding of the corona and is crucial to solving the long-standing problem of coronal heating (Klimchuk 2006). Despite the tremendous efforts made with different techniques over the past two decades, a reliable quantitative measurement of the magnetic flux density of coronal loops remains a central problem in solar (and stellar) physics (Judge et al. 2001; Wiegmann et al. 2014; Casini et al. 2017).

Gyro-resonance emission is an effective method for measuring the magnetic field over ARs of the Sun and some stars (Brosius & White 2006). However, the radio observations are restricted by modest spatial resolution compared with methods in the visible and near-infrared, they can only be

applied at high magnetic field strengths (>100 G) to overcome free-free opacity, and their formation height is not determined by the data themselves. Indirect methods include coronal seismology, which relies on observations of magnetohydrodynamic (MHD) waves to infer the properties of the magnetic field (Nakariakov & Verwichte 2005; Tomczyk et al. 2007). These methods also depend on the assumed nature of the wave modes (local tube modes versus genuine Alfvén waves in more homogeneous media). The most powerful magnetic diagnostics of solar and astrophysical plasmas are based on measurements of the polarized states of light described by the Stokes profiles (I , Q , U , V). Despite its promise (Lin et al. 2000, 2004; Judge et al. 2001), solar coronal polarimetry is extremely difficult due to the inherently low signal-to-noise ratios (S/Ns; the corona is, at best, a million times dimmer than the photosphere). To improve the signal, a coarse spatial (5000–10000 km) and temporal (30–60 minutes) resolution has been used with small instruments in the past (Lin et al. 2000, 2004). However, the highly inhomogeneous corona requires high spatial resolution and the highly dynamic nature of many coronal processes, such as reconnection/diffusion, requires high temporal resolution. Current instrumentation can only achieve high-resolution polarimetric measurements during certain favorable conditions. During solar flares, material evaporates from the chromosphere to the corona and subsequently condenses and falls back to the surface along loops in the form of coronal rain. The high density and lower temperature (due to a lack of sustained heating) permits the use of chromospheric diagnostic transitions as the plasma falls and traces out otherwise “coronal” field lines (Schad et al. 2016; Libbrecht et al. 2019).



Original content from this work may be used under the terms of the [Creative Commons Attribution 3.0 licence](https://creativecommons.org/licenses/by/3.0/). Any further distribution of this work must maintain attribution to the author(s) and the title of the work, journal citation and DOI.

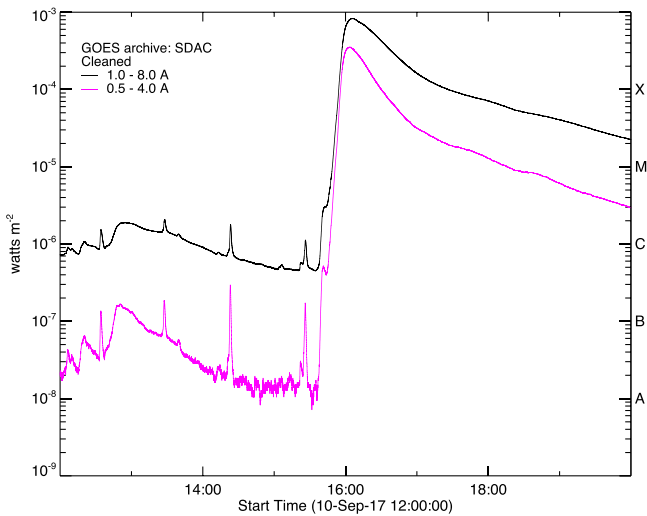


Figure 1. GOES X-ray light curve of the X8.2 class flare of 2017 September 10.

In 2017 September, AR 12673 produced the most powerful flares of solar cycle 24 as it was rotating from disk center to the limb. On 2017 September 10, the AR was just behind the west limb when it produced an X8.2-class flare (SOL2017-09-10T16:06 UT) (Figure 1). Here, we report on the unique observations of the flaring coronal loops during this event at the solar limb using high-resolution imaging spectropolarimetry in the line of singly ionized calcium at 8542.1 Å, from the Swedish 1 m Solar Telescope. The vantage position, orientation, and nature of the chromospheric material that filled the flare loops allowed us to determine their magnetic field with unprecedented accuracy using weak-field approximation (WFA) method.

2. Observations and Data Reduction

The target of our observations was NOAA AR 12673, which produced a series of very energetic flares between 2017 September 1 and 10. The AR was observed between 16:07:21 and 17:58:37 on 2017 September 10 when it was close to the west limb, with heliocentric coordinates of the center of the field of view (FOV) at the beginning of the observations [947", -138"]. Our observations commenced 1 minute after the X8.2 flare peak (~16:06 UT). The observations were carried out with the CRISP Imaging Spectropolarimeter (CRISP; Scharmer 2006; Scharmer et al. 2008) and the CHROMospheric Imaging Spectrometer (CHROMIS) instruments, both based on dual Fabry–Pérot interferometers (FPI) mounted on the Swedish 1 m Solar Telescope (SST; Scharmer et al. 2003) on La Palma. The imaging setup of the SST includes a dichroic beamsplitter (splits at 500 nm), and CRISP is mounted in the resulting red beam and CHROMIS in the blue beam (Löfdahl et al. 2018). The two instruments can collect data simultaneously, but the cameras and scan sequences are not synchronized between them. The CRISP data comprised of imaging spectropolarimetry in the Ca II 8542 Å line consisted of 21 line positions with an irregular step. These positions were -1.75 Å to +1.75 Å (± 1.75 , ± 0.945 , ± 0.735 , ± 0.595 , ± 0.455 , ± 0.35 , ± 0.28 , ± 0.21 , ± 0.14 , ± 0.07 , 0.0 Å) from line core (see the animation associated with Figure 8(a) showing a full spectral scan). Each spectral scan of the Ca II 8542 Å line had an

acquisition time of 16 s but the cadence of the CRISP time series was 33 s due to inclusion of spectropolarimetric scans in the Fe I 6302 Å photospheric line. However, we note that the present paper includes only the analysis of the Ca II 8542 Å data, as the AR, flare loops, and footpoints of these loops were not detected in the Fe I line. The transmission FWHM for Ca 8542 Å line is 107.3 mÅ with a prefilter FWHM of 9.3 Å. Our spatial sampling was 0".057 pixel⁻¹ over the 41 × 41 Mm² FOV.

The data were reconstructed with the Multi-Object Multi-Frame Blind Deconvolution (MOMFBD; Löfdahl 2002; van Noort et al. 2005). We applied the CRISP data reduction pipeline (de la Cruz Rodríguez et al. 2015) for standard data processing. The polarimetric calibration was performed using a linear polarizer and a quarter-wave plate at many different angles close to the primary focus on the optical table. CRISP records four liquid-crystal states per wavelength, which are linear combinations of the Stokes parameters. These states are demodulated to obtain images of the full Stokes vector I , Q , U , and V components using the calibration. For calibrating the CRISP Ca II 8542 Å data, we followed the procedure described in de la Cruz Rodríguez et al. (2013) and used a synthetic Ca II 8542 Å profile computed by a three-dimensional (3D) NLTE radiative transfer code (de la Cruz Rodríguez et al. 2011) and an FTS atlas profile (Neckel 1999) convolved with the CRISP instrumental profile. In order to normalize the data to the continuum intensity, we used a spatially averaged Ca II 8542 Å profile over the 160 × 150 pix² rectangle centered at a quiet-Sun area of $(X, Y) = (34, 4)$ Mm at $\mu \approx 0.15$ (Figure 2).

Figure 2 presents the Ca II 8542 Å Stokes I at $\Delta\lambda = \pm 0.945$ Å and Q , U , and V monochromatic images at $\Delta\lambda = \pm 0.455$ Å at 16:27 UT of the flare loops. The images show that all three polarized Stokes components are detected above the level of background emission. However, the Stokes Q and U profiles are very noisy, and we have not used them for the measurement of the perpendicular component (with respect to the line of sight) of the magnetic field. We note that scattering polarization in Ca II 8542 Å line is expected to be very low, which explains why linear polarizations detected through the CRISP FPI system are weak and noisy in our data (Štěpán & Trujillo Bueno 2016).

We find that most of the Stokes V profiles located in the lower part of the observed loop arcade have a signal around 10^{-2} , and most of the pixels located in the upper parts of the observed loop arcade have a signal above $\sim 1.5 \times 10^{-3}$ in units of continuum intensity I_c . These are above the noise level ($\sim 0.5 \times 10^{-3}$ at the disk and $\sim 0.1 \times 10^{-3}$ above the limb) of these Ca II 8542 Å data.

Simultaneous observations were also taken with the CHROMIS instrument. CHROMIS is a newly installed (2016 August) Fabry–Pérot interferometer that observes the blue part of the spectrum in the range 3900–4900 Å. The CHROMIS observations comprised spectral imaging in the H β 4861 Å and Ca II H 3968.5 and K 3933.7 Å lines, plus one position in the continuum at 4000 Å. The Ca II H and K line scans consist of 19 positions ranging from -1 Å to +1 Å from line core, while the H β scan consists of 21 line positions ranging from -1.2 to +1.2 Å. A full spectral scan for all three lines plus a single continuum position had a total acquisition time of 20 s, which is the temporal cadence of the CHROMIS data time series. The transmission FWHM for the CHROMIS spectrometer

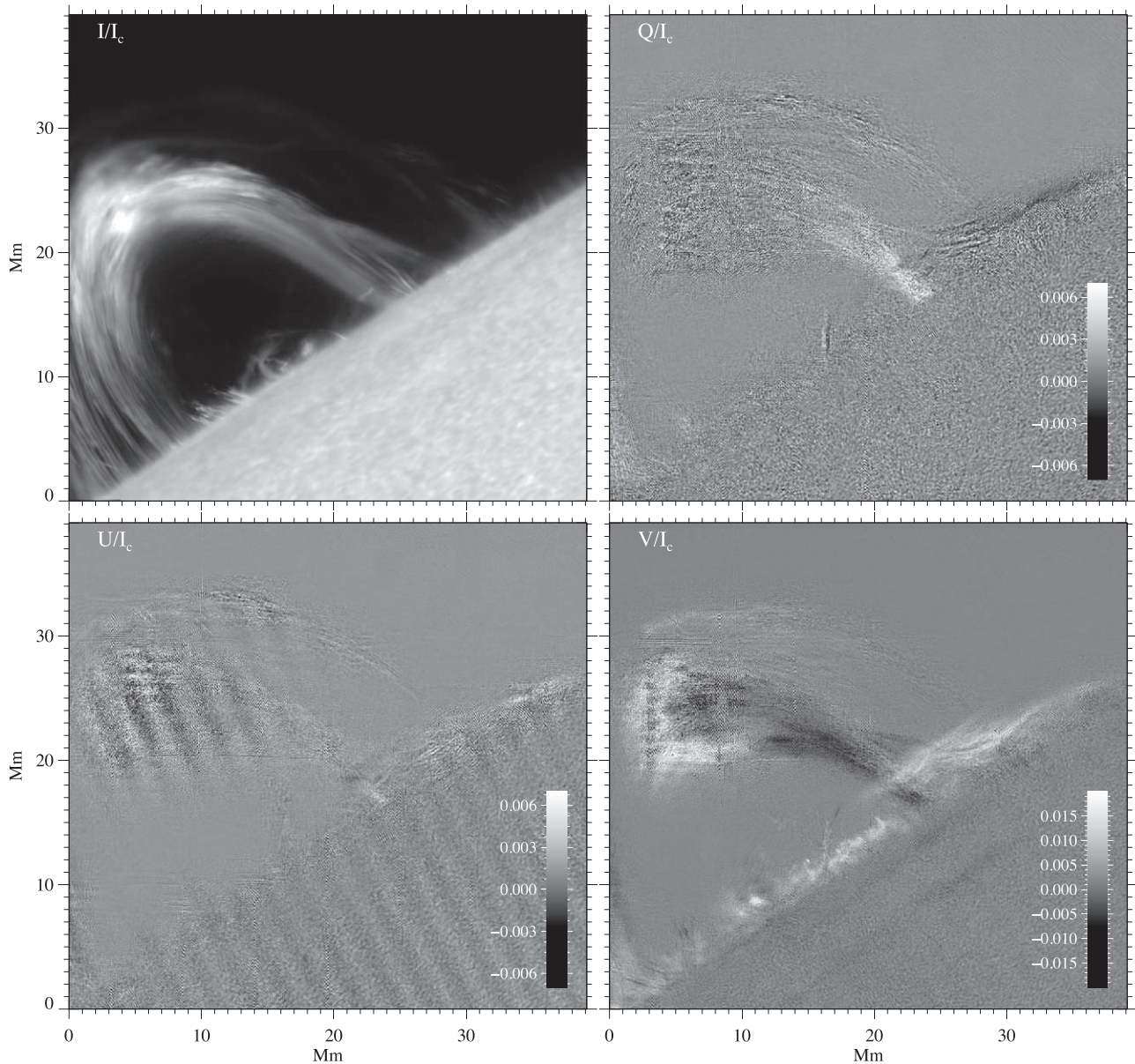


Figure 2. SST images of the flare loops in Ca II 8542 Å Stokes I at $\Delta\lambda = \pm 0.945$ Å and Q , U and V at $\Delta\lambda = -0.455$ Å at 16:27 UT.

(Löfdahl et al. 2018) is 130 mÅ with a spatial sampling of $0''.0375 \text{ pixel}^{-1}$ and a FOV of about $45 \times 30 \text{ Mm}^2$. The CHROMIS data were processed using the CHROMISRED data reduction pipeline (Löfdahl et al. 2018), which includes Multi-Object Multi-Frame Blind Deconvolution image restoration. The pipeline also performs the calibration of the observed intensity in absolute SI intensity units by scaling the spatially averaged spectrum to an atlas profile.

The event was also observed with NASA’s *Solar Dynamics Observatory* (SDO) in the Atmospheric Imaging Assembly (AIA; Lemen et al. 2012) 1600/1700 Å channels (Figure 3; dominated by C IV emission at $\sim 10000 \text{ K}$) and several Extreme-UV channels. Figure 4 shows images from the AIA at 16:29 UT in the He II 304 and Fe IX 171 Å channels with emission from the transition region ($\sim 100,000 \text{ K}$) and corona ($\sim 1,000,000 \text{ K}$). The AIA data was recorded with a cadence of 12 s and spatial sampling of $0''.6 \text{ pixel}^{-1}$. The images are co-aligned with SST/CHROMIS data.

3. Analysis and Results

A well-developed set of flaring coronal loops was observed 10 minutes after the beginning of the impulsive phase of the flare (Figures 3 and 4). The X8.2 flare led to intense heating and evaporation of chromospheric plasma into the loop system. The coronal loops subsequently are filled with dense and cool plasma radiating strongly in chromospheric lines including the magnetically sensitive Ca II 8542 Å (Figures 2–4). We note that the origin of the cool plasma in flare coronal loops is still under debate in the solar community. However, rapid cooling of evaporated plasma through radiation losses is considered as the most plausible explanation of these phenomenon (Klimchuk et al. 1987; Schmieder et al. 1996). Unfortunately, footpoints of the observed flare loops were not detected in SST data, suggesting that they are behind the limb.

The off-limb location of the flare coronal loops minimized contaminations in the chromospheric spectra caused by

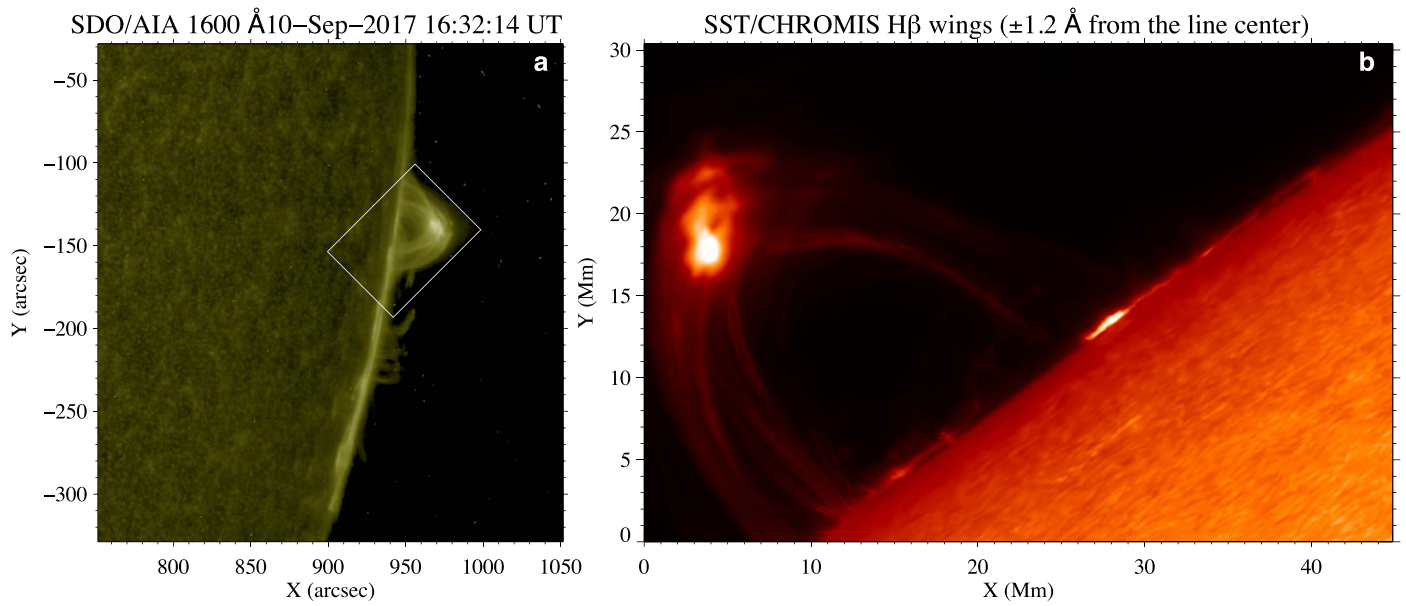


Figure 3. *SDO/AIA* 1600 Å image (a) of AR 12673 near the west limb showing the X8.2 flare coronal loops on 2017 September 10. The SST FOV is outlined with the white box. A composite of SST/CHROMIS $H\beta \pm 1.2$ Å (corresponding to ± 75 km s⁻¹) images (b) of the same flaring loops.

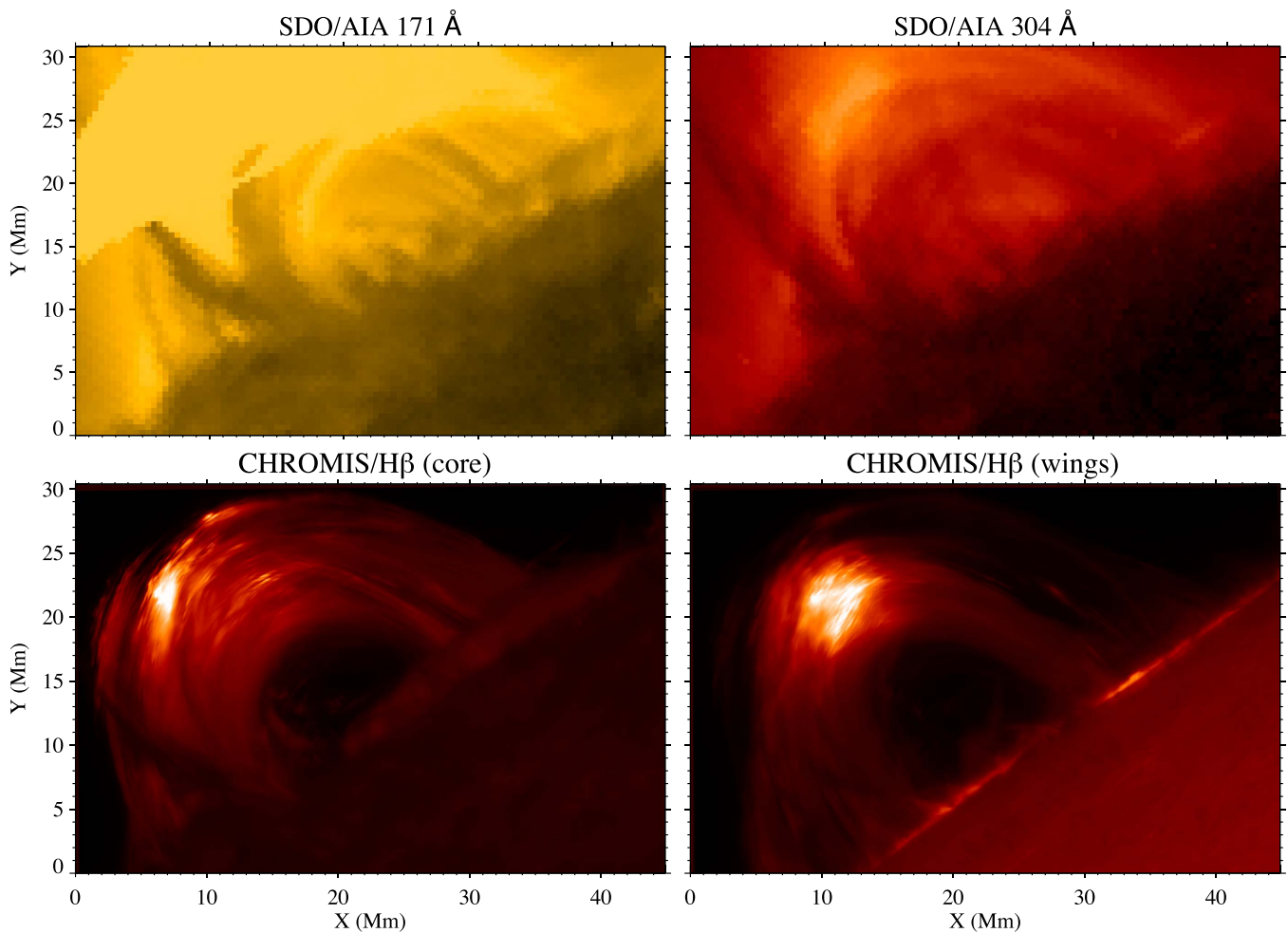


Figure 4. *SDO/AIA* 171 and 304 Å images (top panels) of the X8.2 class solar flare loops on 2017 September 10, 16:29 UT co-aligned with SST/CHROMIS $H\beta$ line core (bottom left panel) and the composite of $H\beta \pm 0.735$ Å (bottom right panel) images.

line-of-sight (LOS) on-disk effects, providing polarization data of unprecedented quality.

3.1. LOS Magnetic Field

3.1.1. Weak-field Approximation

Circular polarization images (Stokes V) of the observed flaring loops acquired in Ca II 8542 Å reveal strong polarization signals along the loops (Figure 2). We use the weak-field approximation (WFA) technique to produce maps of the LOS magnetic field component (B_{LOS}) for the flare coronal loops. The WFA is the simplest approach to calculate the magnetic flux density from the observed line intensity and polarization (Cauzzi et al. 1993; Landi Degl’Innocenti & Landolfi 2004; Asensio Ramos 2011; de la Cruz Rodríguez et al. 2013; Kleint 2017; Centeno 2018; Kuridze et al. 2018). More complex methods such as inversions of polarimetric data are not applicable in this case as they are not optimized for off-limb chromospheric/coronal spectropolarimetric observations. The WFA can provide an accurate estimate of the chromospheric and coronal magnetic field. The main limitation of the WFA is that it can be applied only if the Zeeman splitting ($\Delta\lambda_H$) is much smaller than the Doppler width ($\Delta\lambda_D$) of the observed spectral line (Ca II 8542 Å line in our case) (de la Cruz Rodríguez et al. 2013),

$$\Delta\lambda_H \ll \Delta\lambda_D. \quad (1)$$

Furthermore, the magnetic field and LOS velocity have to be close to a constant as a function of distance along the LOS in the atmosphere. In this regime, the Stokes profiles can be expressed as (Landi Degl’Innocenti & Landi Degl’Innocenti 1977)

$$V(\lambda) = -4.67 \times 10^{-13} g_{\text{eff}} \lambda_0^2 B_{\text{LOS}} \frac{\partial I(\lambda)}{\partial \lambda}, \quad (2)$$

$$[Q^2 + U^2]^{1/2} = \left| -5.45 \times 10^{-26} \bar{G} \lambda_0^4 B_{\perp}^2 \frac{\partial^2 I(\lambda)}{\partial \lambda^2} \right|, \quad (3)$$

where g_{eff} is the first order effective Landé factor, and λ_0 is the central wavelength of the spectral line. \bar{G} is a second-order effective Landé factor related to g_{eff} with

$$\bar{G} = g_{\text{eff}}^2 - (g_1 - g_2)^2 (16s - 7d^2 - 4) / 80, \quad (4)$$

where

$$s = J_1(J_1 + 1) + J_2(J_2 + 1), \quad d = J_1(J_1 + 1) - J_2(J_2 + 1)$$

for the angular momentum J_1 and J_2 of the involved energy levels with Landé factors g_1 and g_2 (Landi Degl’Innocenti & Landi Degl’Innocenti 1977). For Ca II 8542 Å line $g_{\text{eff}} = 1.1$ and $\bar{G} = 1.21$. We note that the units for the wavelength and magnetic field are Å and G, respectively.

The low Landé factor and relatively broader line width due to the increased temperature (compared to photospheric temperature) of Ca II 8542 Å suggests that the WFA is an appropriate method for this line. Under chromospheric conditions, the upper limit of the WFA for the Ca II 8542 Å is estimated to be approximately $B \leq 2500$ G (Asensio Ramos 2011; de la Cruz Rodríguez et al. 2013). The average field strength in the chromosphere and corona are well below this value, so the WFA should be a valid method for inferring the magnetic field using the Ca II 8542 Å line. For most of the pixels in the observed coronal loops, Equation (1) is fulfilled.

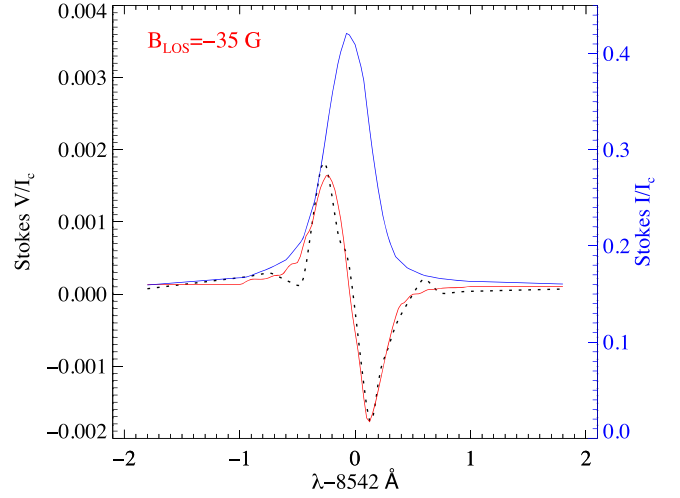


Figure 5. Circular polarization profile (black dashed line) of the pixel with the weakest LOS magnetic field ($X = 15$ Mm, $Y = 30$ Mm in Figure 2) at 16:28 UT. The blue line shows the intensity (Stokes I), and the solid red line shows the WFA fit obtained from the derivative of Stokes I .

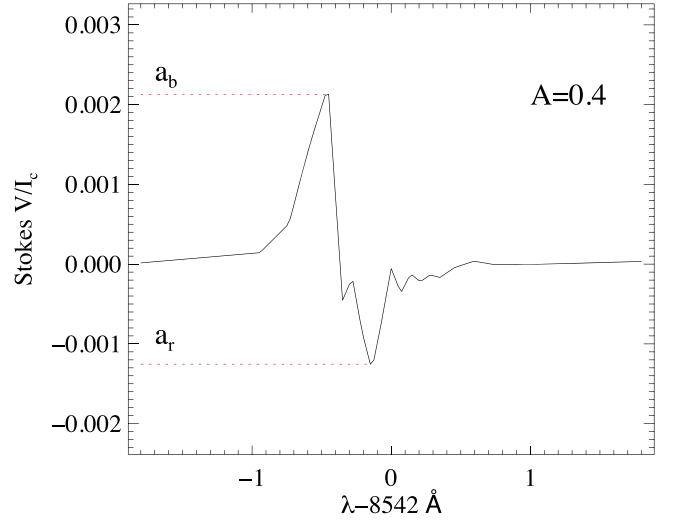


Figure 6. Asymmetric Stokes V profile observed for a pixel located at around $X = 16$ Mm, $Y = 32$ Mm (Figure 2). a_b and a_r denote the red and blue wing amplitudes, which define the amplitude asymmetry, A .

Line profiles that have not met the criterion presented in Equation (1) are excluded from the analysis. Figure 5 shows an example of the Stokes I and V profiles and the WFA fit obtained from the derivative of Stokes I , for the pixel with the weakest LOS magnetic field.

As mentioned above, the WFA is applicable when the magnetic field and velocities are close to a constant along the LOS. The Ca II 8542 line emission is formed over a wide layer of the solar atmosphere, suggesting that due to the vertical stratifications, the magnetic field can have a strong gradient as a function of height in the atmosphere. However, off-limb coronal-loop observations provide less inhomogeneity along the LOS. Magnetic field/velocity gradients and/or discontinuities can produce asymmetric Stokes V profiles (Khomenko et al. 2003). Therefore, asymmetries can be used as a good indicator of magnetic field/velocity gradients.

To quantify the asymmetry of the Ca II 8542 line Stokes V profiles, we use a technique similar to that described in

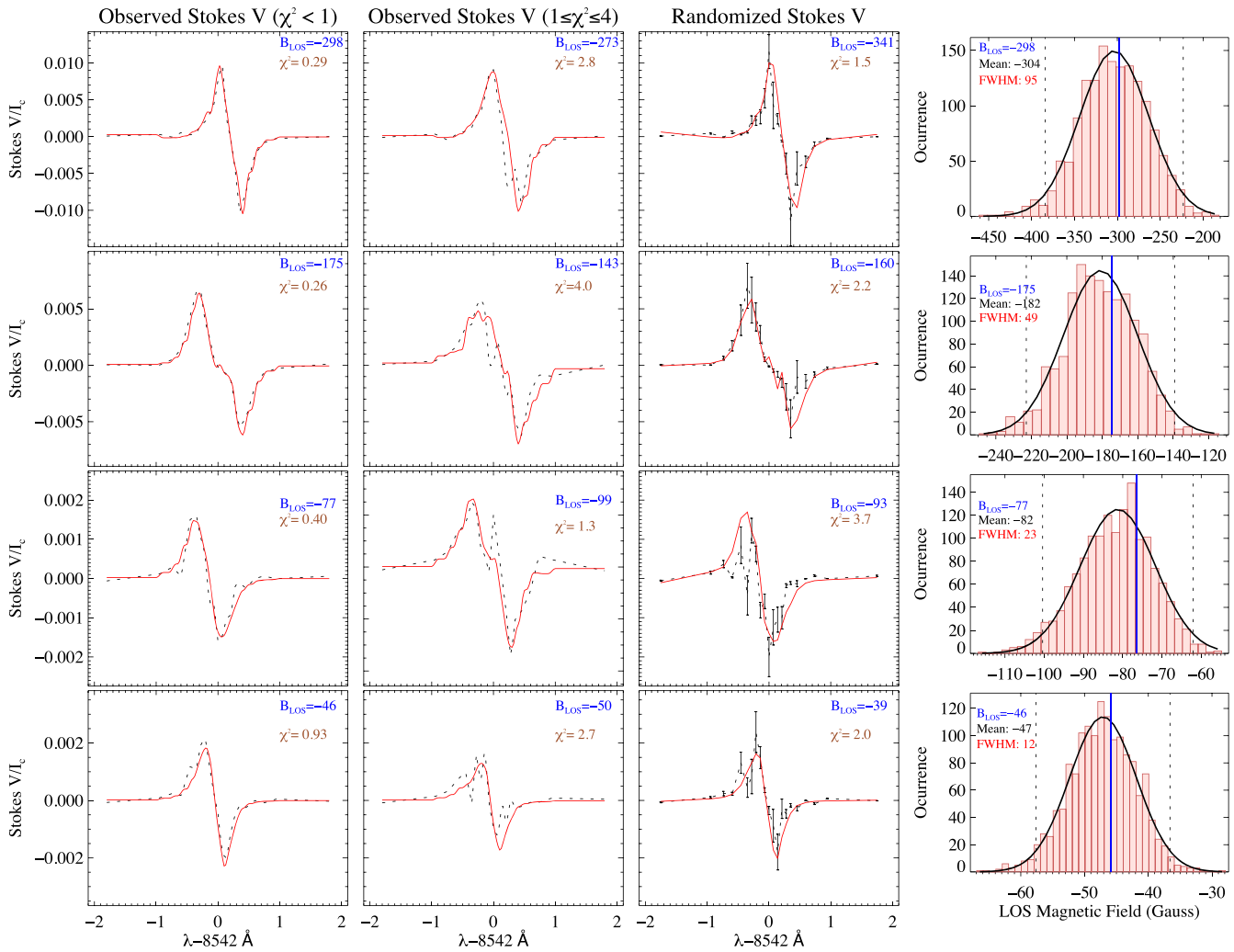


Figure 7. Column 1: observed Stokes V profiles (black dashed lines) in the pixels with the lowest noise level and goodness-of-fit $\chi^2 < 1$. The WFA fits obtained from the derivative of Stokes I are depicted as solid red lines. Column 2: typical Stokes profiles with higher noise level and goodness-of-fit with $1 \leq \chi^2 \leq 4$. Column 3: randomized Stokes V profiles presented in the column 1. The randomization degrades their WFA goodness-of-fit to $1 \leq \chi^2 \leq 4$. Column 4: histograms of the magnetic field strength values derived with the WFA from the derivative of the randomized Stokes I and Stokes V presented in the third column. The vertical blue solid line on each histogram indicates the values of B_{LOS} computed with the WFA before randomization of the Stokes V and I . Error bars represent standard deviation values from the 1500 randomization. Gaussian fits of the histograms are presented as the full black lines with the 95% confidence intervals (the vertical dashed lines).

Sigwarth (2001). We measured the absolute values of amplitudes of the red and blue lobes, a_b and a_r , respectively, for every pixel in the observed coronal loops and compute amplitude asymmetry with

$$A = \frac{|a_b - a_r|}{\max(a_r, a_b)}. \quad (5)$$

$A = 0$ corresponds to no amplitude asymmetries in the Stokes V line profiles and $A = 1$ corresponds to maximum asymmetry, which is the case when Stokes V has a single lobe profile. Figure 6 shows an asymmetric Stokes V profile with $A = 0.4$. Profiles with asymmetry higher than 0.4 were excluded from the analysis. This value was chosen based on a statistical analysis of randomized profiles (see Section 3.1.3) indicating that the asymmetries below this value are very likely introduced by the noise rather than by the gradients in magnetic field and velocity (Figure 7).

Equation (2) shows that $\partial I(\lambda)/\partial \lambda$ can be used as a calibration constant for the LOS magnetic field component. To extend the wings of the observed Stokes profiles, we added

two more wavelength points at $\pm 1.8 \text{ \AA}$ and extrapolated the profiles at these points. Stokes profiles were also averaged over $0''.23 \times 0''.23$ ($\sim 170 \text{ km}$) area in order to improve S/N. The derivatives of Stokes I were then calculated with IDL's built-in deriv function for every pixel of the observed coronal loops. Then, the best fit between the $V(\lambda)$ and $\partial I/\partial \lambda$ is computed with the least-square minimization technique. The fitting coefficient directly gives the values for the magnetic field. The parameter χ^2 that characterizes the discrepancies (goodness-of-fit) between Stokes V and the derivatives was also computed for every pixel. Figure 7 (first and second columns) shows Stokes V profiles from different parts of the observed coronal loops, together with the WFA fits obtained from the derivative of Stokes I (overplotted as solid red lines). The first column of Figure 7 shows the results for lower χ^2 (< 1) and the second column shows the results with higher χ^2 ($\sim 1-4$).

Figure 8(c) shows the resulting map of the LOS magnetic field, across large regions of the loop system. The histograms in Figure 8(d) are the distributions of the LOS magnetic field for three different height ranges. B_{LOS} of the loop apex region (layer

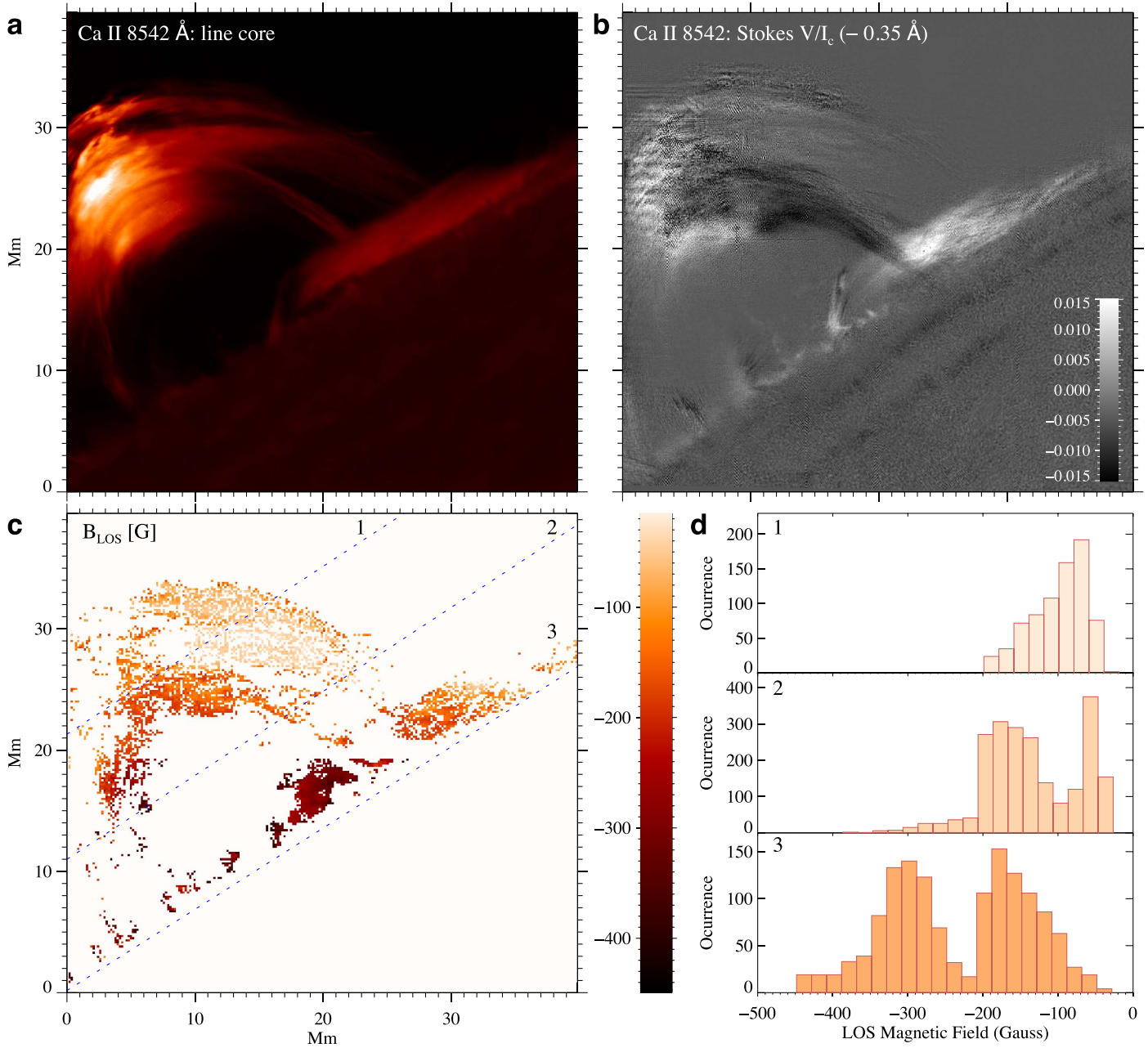


Figure 8. Panels (a) and (b) show the SST images in the Ca II 8542 Å intensity (Stokes I) at line core and circular polarization (Stokes V) at line wing for the flare coronal loops at 16:28 UT, 22 minutes after the flare peak. Panels (c) and (d) show a map of the LOS magnetic field together with histogram showing the distribution of the LOS magnetic fields for three different regions (1, 2, 3). An animation of panel (a) is available. The video duration is 10 s and it shows the flare image and the scan across the line. The inset in the animation shows the line in velocity space.

(An animation of this figure is available.)

1, between 18 and 26 Mm above the solar surface) ranges from 50 to 180 G with median 90 G. The corresponding values at mid-heights (layer 2, 9 to 18 Mm) are as high as 300 G with a median of 140 G. The polarization signal of the loop legs in the lower part of the FOV (layer 3, up to 9 Mm) is very weak due to the increased perpendicular orientation of the loop legs. Layer 3 is also contaminated by a solar prominence associated with the flare, lying along the LOS. The distribution of the LOS magnetic field here shows two distinct peaks at 150 and 300 G.

Compared to the LOS component, it is more challenging to compute the perpendicular component of the magnetic field with the WFA fitting, as it is related to the total linear polarization,

which depends on the second derivative of Stokes I with respect to wavelength (Equation (3)). The measured linear polarization signals (Stokes Q and U) are noisy and could not be used to estimate the component of the magnetic field that is perpendicular to our LOS under the WFA limit (Equation (3)).

3.1.2. Influence of Spectral Sampling

L. Kleint & A. Sainz Dalda (2015, private communication) have investigated the influence of the spectral sampling on the WFA for the Ca II 8542 Å line by synthesizing the line in Non-local Thermodynamical Equilibrium (NLTE), with the NICOLE inversion code (Socas-Navarro et al. 2015). They used different

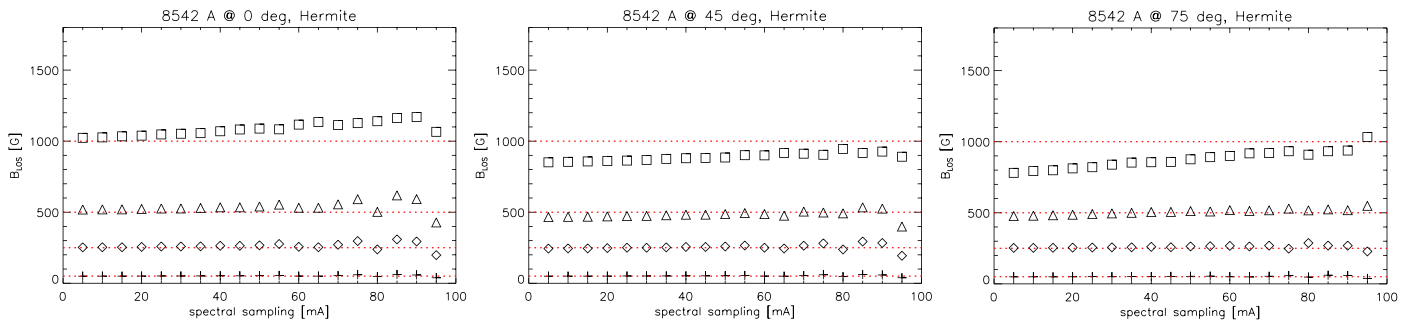


Figure 9. Magnetic field values derived from the WFA for different spectral samplings for the synthetic Ca II 8542 Å data. The input fields are denoted by horizontal dotted lines and the calculated values with the WFA are given by the various symbols (+: 50 G, diamond: 250 G, triangle: 500 G, box: 1000 G). The left panel shows a purely vertical magnetic field, the middle panel a field with inclination 45° and the right panel a field with inclination 75° with respect to the solar surface, which influences the errors of the derived values.

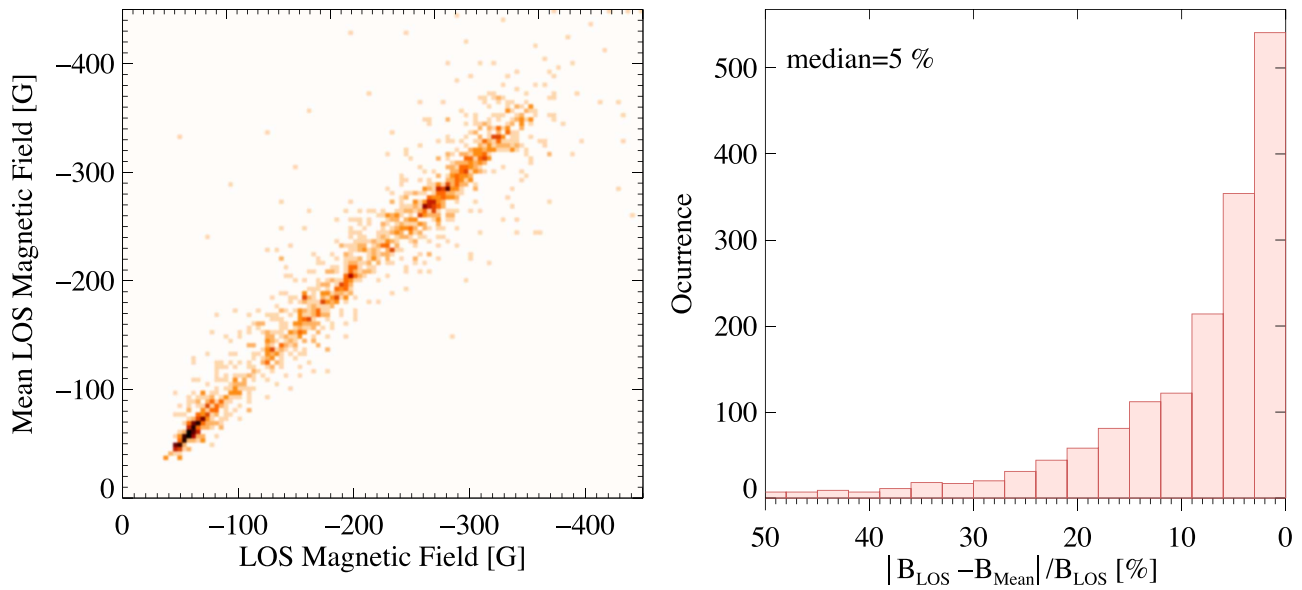


Figure 10. Scatter plot represented as a two-dimensional density map of the LOS magnetic field measured from the WFA of the initial, high-quality Stokes profiles vs. the mean B_{LOS} retrieved after the randomization test.

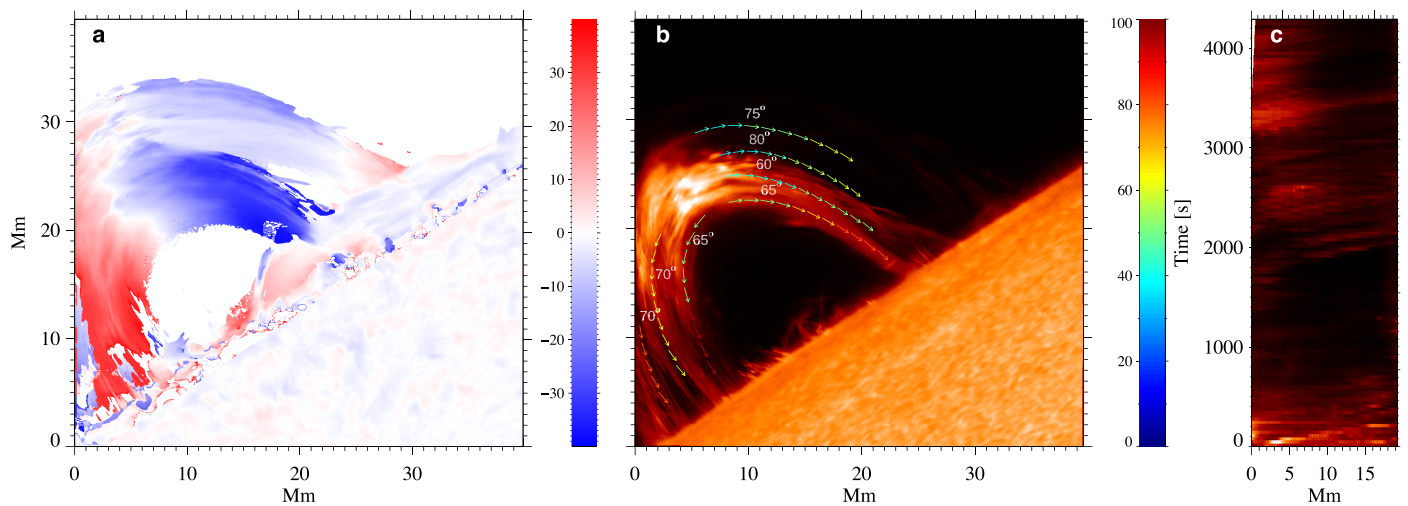


Figure 11. (a) Doppler map of the flaring coronal loops. (b) Composite of CRISP Ca II 8542 ± 0.945 Å images. The color-coded arrows indicate direction and speed of plasma flows. The numbers above the arrows indicate average viewing angles of the flow/magnetic loops with respect to the LOS direction. The color bars give velocity in km s^{-1} . (c) Time-distance diagram of Ca 8542 ± 0.945 Å intensity along the outermost arrows in panel (b).

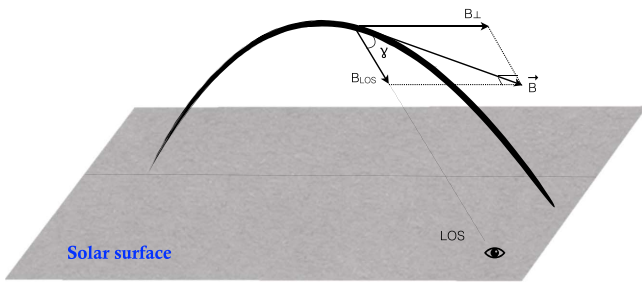


Figure 12. Schematic representation of the magnetic loop showing the basic geometry, magnetic field vector and its LOS and perpendicular components with respect to the observer.

input values (between 50 and 1000 G) for the LOS magnetic field and computed synthetic profiles for different spectral sampling (from 5 to 100 mÅ), model atmospheres (VAL-C and HSRA), and predefined inclinations. The B_{LOS} was then computed with the WFA and the results were compared to the original input magnetic field values to estimate the influence of spectral sampling on the WFA. Figure 9 shows that the difference between input values and derived magnetic fields generally increases when the spectral sampling increases for a kG field. However, for fields ≤ 500 G, there is a very good match between them even for large spectral sampling. The B_{LOS} derived in the present work with the WFA are below 400 G and the spectral sampling of our data near the line core is 70 mÅ. This suggests that in locations with well-defined Stokes profiles with a good fit between Stokes V and the derivative of Stokes I , the WFA provides a very accurate measure of the magnetic field density, with error smaller than 10%.

3.1.3. Uncertainty of the Measurement

A large fraction (20%) of the pixels selected for this analysis and presented in the LOS magnetic map (Figure 8(c)) have well-defined, regular, symmetric Stokes V profiles with $\chi^2 \leq 1$. Examples of such profiles are presented in Figure 5 and the first column of Figure 7. As it was discussed in Section 3.1.2, for such profiles, the estimated error of the measured magnetic field strength is less than 10%. Typical profiles with higher noise level and hence higher goodness-of-fit ($1 \leq \chi^2 \leq 4$) for the WFA are shown in the second column of Figure 7. Profiles with $\chi^2 > 4$ were ignored and are not included in the magnetic field map (Figure 8). To estimate an influence of the noise on the B_{LOS} values derived by the WFA we performed randomization tests. The method has been applied in the following way: we chose the three best scans from our time series in terms of spatial resolution. From each selected scan, we chose the pixels with the Stokes V and I profiles with the lowest noise level and lowest WFA goodness-of-fit ($\chi^2 \leq 1$). For these pixels, we applied artificial noise by using a randomization of the Stokes V and I profiles and degraded their WFA goodness-of-fit to $1 \leq \chi^2 \leq 4$. The third column of Figure 7 shows the Stokes V profiles produced by such randomization from the profiles presented in the first column of Figure 7. The process is repeated 1500 times for each selected pixel, producing a distribution of values for the LOS magnetic field. The right column of Figure 7 shows the histograms of the magnetic field values derived with the WFA after randomization of Stokes V profiles with the lowest noise level (presented in the left column of Figure 7). The vertical solid blue lines on

each histogram indicate the values of B_{LOS} computed with the WFA before randomization of the Stokes V and I .

The left panel of Figure 10 shows the density map of the LOS magnetic field measured from the WFA of the initial, high-quality Stokes profiles versus the mean, B_{Mean} retrieved after the randomization test. The right panel of Figure 10 shows that the relative error of the B_{Mean} compared to the original B_{LOS} obtained from the WFA is around 5%. This suggests that the upper limit of the uncertainty of the LOS magnetic field derived from the WFA for the profiles with goodness-of-fit $1 \leq \chi^2 \leq 4$ should be close to the 2σ uncertainty ranges, which is less than 30% of B_{Mean} (Figure 7).

3.2. Velocity Map

The line profiles are fitted with Gaussian functions to determine the bulk plasma LOS velocity (Figure 11(a)). Most of the CRISP/Ca II 8542 Å line profiles are well-defined, single peaked emission profiles. However, many pixels ($\sim 40\%$) of the coronal loops in the CHROMIS/Ca K and H and H β lines have irregular, noisy profiles, and they cannot be fitted reliably with a single Gaussian. As CHROMIS covers the shorter wavelengths, it is more susceptible to seeing conditions compared to CRISP, and changes in atmospheric seeing during the scan time of spectral lines has affected the quality of some of the CHROMIS data. The Doppler velocities measured for the pixels with the well-defined profiles in CHROMIS lines are consistent with the velocities obtained from the CRISP Ca II 8542 Å line indicating the reliability of the measurements. Mapping this value (Dopplergrams) reveals that the left and right parts of the loop structures contain regions of red and blueshifted profiles, respectively, with velocities between ~ 10 – 35 km s $^{-1}$ (Figure 11(a)). Time–distance diagrams show strong gravity-driven downflows of dense and cool plasma from the loop apex toward the footpoints. These apparent plane of sky (POS) velocities range between 50 and 100 km s $^{-1}$ (Figures 11(b) and (c)). The apparent and Doppler velocities are almost zero near the loop apex and increase toward the footpoints (Figures 11(b) and (c)). These velocities are the two orthogonal—LOS (V_{LOS} , Dopplergrams) and POS (V_{POS} , apparent) components of the downflowing plasma motions with respect to the observer.

We note that line profiles of bright loop top seen in Ca II and H β images (Figures 3, 4, 8, 11(b)) have a very strong central reversal. This bright top is formed through the accumulation of evaporated plasma, and it can have higher density and optical depth compared to loop legs, which explains why its line profiles show a central reversal (Kuridze et al. 2015, 2016, 2017). We will investigate the density structure of this loop top and formation of central reversal in the follow-up study.

As we mentioned above, the loop footpoints are no longer visible because they have rotated to the far side of the Sun. However, the downflows from the loop apex toward the footpoints produce blueshifts above the rightmost footpoint and redshift above the leftmost footpoint (Figure 11(a)). This suggests that the right-hand footpoint is located nearer to an observer. The measured B_{LOS} is negative everywhere along the loops, suggesting that the left footpoint of this arcade has positive polarity and right one has negative.

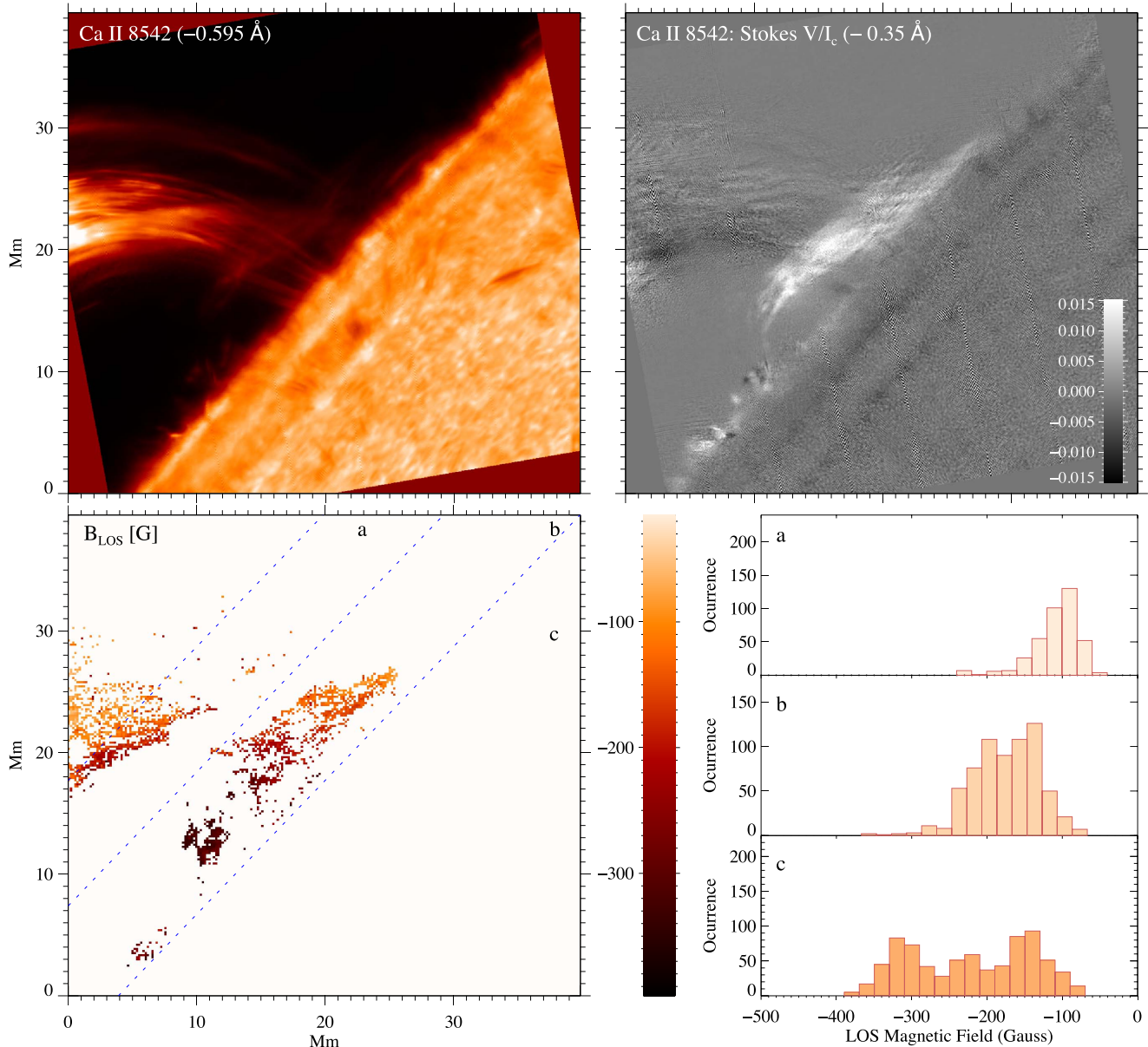


Figure 13. Same as Figure 8 obtained 5 minutes later at 16:33 UT.

3.3. Magnetic Flux Density

Since the moving plasma must obey Alfvén’s theorem on the scales observed (i.e., be frozen in loops or perhaps in sheets separating them), the direction of flow velocity follows the direction of the magnetic loops. The viewing angle, γ , of the magnetic field and velocity with respect to the observer, (Figure 12), can be determined from the ratio between the LOS and perpendicular components of either the magnetic field or velocity vectors. In contrast to the LOS component, it is impossible with given noise levels to compute the perpendicular component of the magnetic field with the WFA fitting as it is related to the total linear polarization, which depends on the second derivative of Stokes I (see Equation (3)). The measured linear polarization signals are noisy and cannot be used to estimate the field component that is perpendicular to our LOS. The ratio of $V_{\text{POS}}/V_{\text{LOS}}$ at different parts of the loop system ranges between 1.7 and 4, showing that the dominant component of the downflow

motion and hence the magnetic field is the component perpendicular to the LOS (Figures 11(b) and 12). The average viewing angle of the velocity vectors computed from these ratios is approximately $\gamma \approx 60\text{--}80$ degrees (Figures 11(b) and 12). This yields a median of total magnetic flux density, $B_{\text{TOT}} \sim B_{\text{LOS}}/\cos\gamma$ (Figure 12), of around 350 G at the apex of the loop system (region 1 in Figure 8(c)), and 420 G at mid-heights (region 2 in Figure 8(c)).

4. Discussion and Conclusion

Here we present two-dimensional (2D) maps of the magnetic field of a full coronal-loop system using chromospheric spectropolarimetry with unprecedented spatiotemporal resolution. This is a unique observation with its associated results for the following reasons: (i) the flare took place when the AR was at the West limb, a vantage position that allowed us to see the plasma rise from the chromosphere to coronal heights; (ii) we

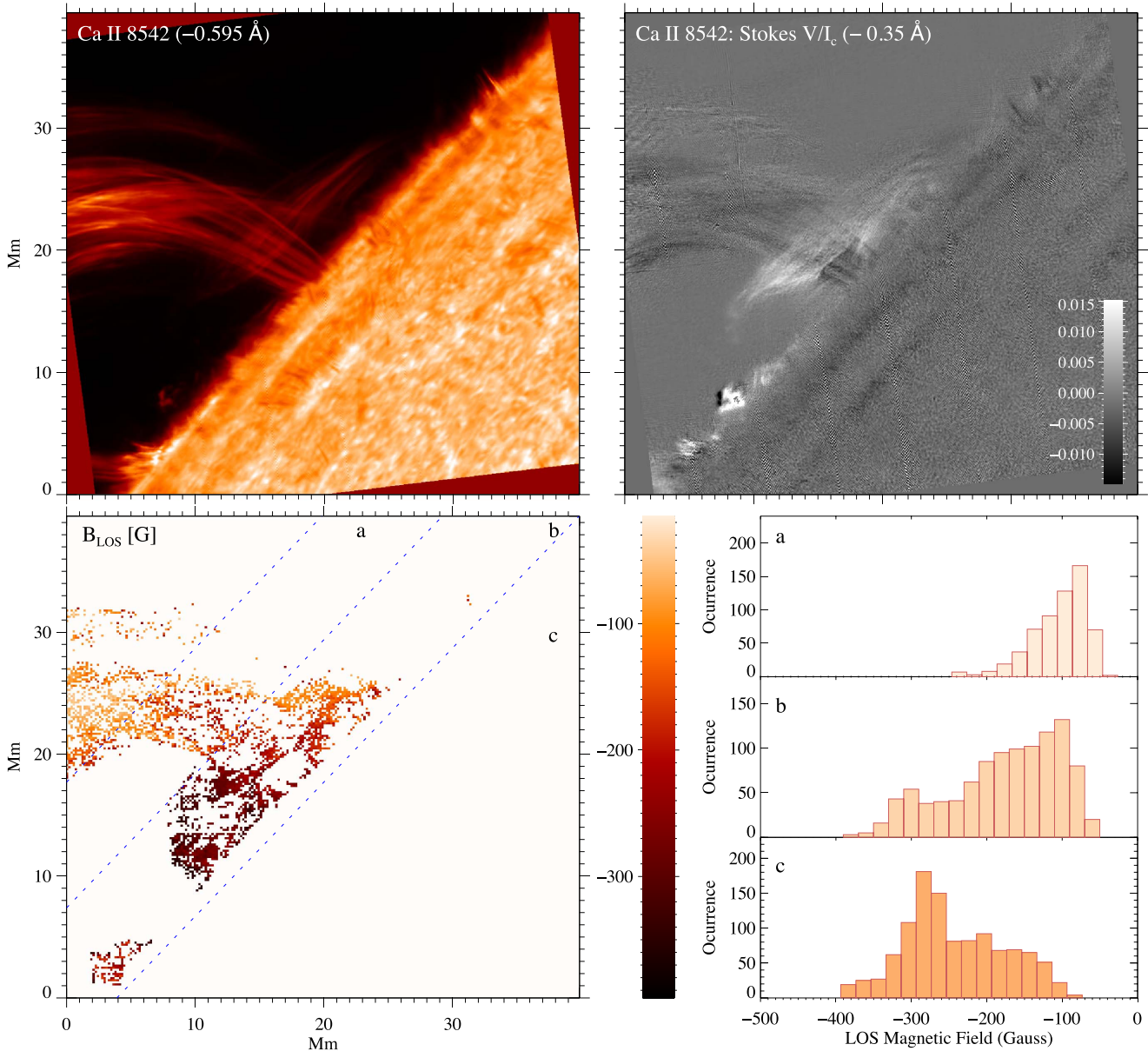


Figure 14. Same as Figures 8 and 13 just at 16:45 UT.

were able to overcome the challenges posed by the weak signal of coronal lines by using a chromospheric diagnostic at coronal heights; (iii) our observations and magnetic field measurements achieved an unprecedented spatial (~ 170 km) and temporal (~ 16 s) resolution up to a height of 25 Mm into the corona; (iv) the high signal allows us to apply the WFA, which is straightforward and does not involve elaborate assumptions or modeling. Yet it provides an accurate estimate of the coronal magnetic field.

Our analysis reveals coronal magnetic field strengths as high as 350 G at heights up to 25 Mm above the solar limb. These values are considerably higher than previous estimates for the coronal field obtained with low-resolution spectropolarimetry and coronal magnetoseismology (Lin et al. 2000, 2004; Nakariakov & Verwichte 2005; Tomczyk et al. 2007). To estimate the effect of spatial and temporal resolution on the measurement of the magnetic field we degraded our data to $1''.5$ and repeated the measurements. Compared to the original

high-resolution data, the LOS magnetic flux density is underestimated by $\sim 70\%$ – 80% along different parts of the loops, which partly explains the low values reported in previous works.

The temporal evolution of the magnetic field maps shows no significant changes over the 30-minute period (between 16:28 and 16:45 UT) (Figures 8, 13, and 14), indicating that the loops remain stable even in the aftermath of a large flare, and despite the large mass flux along the loops. We note that a complementary study using white light data from the HMI instrument on board *SDO* shows that the density of these post flare loops are around 10^{13} cm^{-3} (Jejčić et al. 2018) which is almost two orders of magnitude higher than typical coronal-loop densities (Young et al. 2009).

This first high-resolution measurement of the magnetic field strength of solar coronal loops represents a major step forward in understanding coronal magnetism. The observations and analysis prove that, under certain circumstances, the high-resolution

spectropolarimetry of the Ca II 8542 Å line gives an accurate measure of the coronal field. This constraint is crucial for physical models of coronal ARs, flares and eruptions, and provides a validation of widely used numerical methods for the extrapolation of photospheric magnetic fields in the corona. Furthermore, the result is important for upcoming new-generation ground-based solar telescopes such as 4 m Daniel K. Inouye Solar Telescope (DKIST) and European Solar Telescope (EST; first lights in 2020 and 2027, respectively). These telescopes will have advanced chromospheric polarimetric capabilities, which, as demonstrated here, can provide powerful diagnostics for the coronal magnetic field.

The research leading to these results has received funding from the Sêr Cymru II Part-funded by the European Regional Development Fund through the Welsh Government. The Swedish 1 m Solar Telescope is operated on the island of La Palma by the Institute for Solar Physics of Stockholm University in the Spanish Observatorio del Roque de los Muchachos of the Instituto de Astrofísica de Canarias. The Institute for Solar Physics is supported by a grant for research infrastructures of national importance from the Swedish Research Council (registration number 2017-00625). D.K., M.M., and A.R. acknowledge support from STFC under grant No. ST/P000304/1. The work of D.K. was supported by Georgian Shota Rustaveli National Science Foundation project FR17_323. R.O. acknowledges support from MINECO and FEDER funds through projects AYA2014-54485-P and AYA2017-85465-P. J.K. acknowledges the project VEGA 2/0004/16. This article was created by the realization of the project ITMS No. 26220120029, based on the supporting operational Research and development program financed from the European Regional Development Fund. T.V.Z. was supported by the Austrian Science Fund (FWF), project 30695-N27. We would like to thank the referee Dr Philip Judge for comments and suggestions that help us improve the presentation of the results in this manuscript.

ORCID iDs

D. Kuridze  <https://orcid.org/0000-0003-2760-2311>
 M. Mathioudakis  <https://orcid.org/0000-0002-7725-6296>
 R. Oliver  <https://orcid.org/0000-0003-4162-7240>
 L. Kleint  <https://orcid.org/0000-0002-7791-3241>
 J. Koza  <https://orcid.org/0000-0002-7444-7046>

References

- Asensio Ramos, A. 2011, *ApJ*, **731**, 27
 Brosius, J. W., & White, S. M. 2006, *ApJL*, **641**, L69
 Casini, R., White, S. M., & Judge, P. G. 2017, *SSRv*, **210**, 145
 Cauzzi, G., Smaldone, L. A., Balasubramaniam, K. S., & Keil, S. L. 1993, *SoPh*, **146**, 207
 Centeno, R. 2018, *ApJ*, **866**, 89
 de la Cruz Rodríguez, J., Kiselman, D., & Carlsson, M. 2011, *A&A*, **528**, A113
 de la Cruz Rodríguez, J., Löfdahl, M. G., Sütterlin, P., Hillberg, T., & Rouppe van der Voort, L. 2015, *A&A*, **573**, A40
 de la Cruz Rodríguez, J., Rouppe van der Voort, L., Socas-Navarro, H., & van Noort, M. 2013, *A&A*, **556**, A115
 Jejič, S., Kleint, L., & Heinzel, P. 2018, *ApJ*, **867**, 134
 Judge, P. G., Casini, R., Tomczyk, S., Edwards, D. P., & Francis, E. 2001, STIN, Tech. Rep., **PB2002-102493**
 Khomenko, E. V., Collados, M., Solanki, S. K., Lagg, A., & Trujillo Bueno, J. 2003, *A&A*, **408**, 1115
 Kleint, L. 2017, *ApJ*, **834**, 26
 Klimchuk, J. A. 2006, *SoPh*, **234**, 41
 Klimchuk, J. A., Antiochos, S. K., & Mariska, J. T. 1987, *ApJ*, **320**, 409
 Kuridze, D., Henriques, V., Mathioudakis, M., et al. 2017, *ApJ*, **846**, 9
 Kuridze, D., Henriques, V. M. J., Mathioudakis, M., et al. 2018, *ApJ*, **860**, 10
 Kuridze, D., Mathioudakis, M., Christian, D. J., et al. 2016, *ApJ*, **832**, 147
 Kuridze, D., Mathioudakis, M., Simões, P. J. A., et al. 2015, *ApJ*, **813**, 125
 Landi Degl'Innocenti, E., & Landi Degl'Innocenti, M. 1977, *A&A*, **56**, 111
 Landi Degl'Innocenti, E., & Landolfi, M. 2004, *Astrophysics and Space Science Library*, Vol. 307, *Polarization in Spectral Lines* (Dordrecht: Kluwer), 1
 Lemen, J. R., Title, A. M., Akin, D. J., et al. 2012, *SoPh*, **275**, 17
 Libbrecht, T., de la Cruz Rodríguez, J., Danilovic, S., Leensaarts, J., & Pazira, H. 2019, *A&A*, **621**, A35
 Lin, H., Kuhn, J. R., & Coulter, R. 2004, *ApJL*, **613**, L177
 Lin, H., Penn, M. J., & Tomczyk, S. 2000, *ApJL*, **541**, L83
 Löfdahl, M. G. 2002, *Proc. SPIE*, **4792**, 146
 Löfdahl, M. G., Hillberg, T., de la Cruz Rodríguez, J., et al. 2018, arXiv:1804.03030
 Nakariakov, V. M., & Verwichte, E. 2005, *LRSP*, **2**, 3
 Neckel, H. 1999, *SoPh*, **184**, 421
 Schad, T. A., Penn, M. J., Lin, H., & Judge, P. G. 2016, *ApJ*, **833**, 5
 Scharmer, G. B. 2006, *A&A*, **447**, 1111
 Scharmer, G. B., Bjelksjö, K., Korhonen, T. K., Lindberg, B., & Pettersson, B. 2003, *Proc. SPIE*, **4853**, 341
 Scharmer, G. B., Narayan, G., Hillberg, T., et al. 2008, *ApJL*, **689**, L69
 Schmieder, B., Heinzel, P., van Driel-Gesztelyi, L., & Lemen, J. R. 1996, *SoPh*, **165**, 303
 Sigwarth, M. 2001, *ApJ*, **563**, 1031
 Socas-Navarro, H., de la Cruz Rodríguez, J., Asensio Ramos, A., Trujillo Bueno, J., & Ruiz Cobo, B. 2015, *A&A*, **577**, A7
 Štěpán, J., & Trujillo Bueno, J. 2016, *ApJL*, **826**, L10
 Tomczyk, S., McIntosh, S. W., Keil, S. L., et al. 2007, *Sci*, **317**, 1192
 van Noort, M., Rouppe van der Voort, L., & Löfdahl, M. G. 2005, *SoPh*, **228**, 191
 Wiegmann, T., Thalmann, J. K., & Solanki, S. K. 2014, *A&ARv*, **22**, 78
 Young, P. R., Watanabe, T., Hara, H., & Mariska, J. T. 2009, *A&A*, **495**, 587